Journal of Colloid and Interface Science 554 (2019) 142–156

Contents lists available at ScienceDirect

Journal of Colloid and Interface Science

journal homepage: www.elsevier.com/locate/jcis

Regular Article

Preparation of starch-based porous carbon electrode and biopolymer electrolyte for all solid-state electric double layer capacitor

Palanisamy Rupa Kasturi [a], Harivignesh Ramasamy [b], Danielle Meyrick [c], Yun Sung Lee [b], Ramakrishnan Kalai Selvan [a,*]

[a] Energy Storage and Conversion Devices Laboratory, Department of Physics, Bharathiar University, Coimbatore 641046, Tamil Nadu, India
[b] Faculty of Applied Chemical Engineering, Chonnam National University, Gwangju 500-757, South Korea
[c] Departments of Nuclear Medicine, The University of Western Australia, School of Medicine, Perth, Australia

GRAPHICAL ABSTRACT

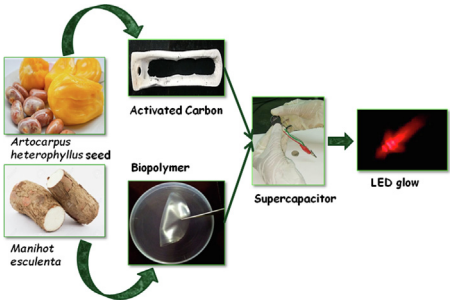

ARTICLE INFO

Article history:
Received 22 April 2019
Revised 8 June 2019
Accepted 24 June 2019
Available online 25 June 2019

Keywords:
Artocarpus heterophyllus seed starch
Activated porous carbon
Biopolymer electrolyte
Supercapacitor

ABSTRACT

An ever-increasing demand for energy coupled with environmental pollution associated with conventional energy production continues to drive the search for alternative renewable energy storage solutions. In this regard, a high surface area (1841 $m^2 g^{-1}$), hierarchically porous (~1.18 $cm^3 g^{-1}$) and self-inherited nitrogen (2.1 at.wt%) based activated carbon are obtained from *Artocarpus heterophyllus* seed derived starch as a result of $ZnCl_2$ chemical activation. A flexible, conductive, thermally stable and biodegradable biopolymer electrolyte film is prepared from *Manihot esculenta* starch powder. These eco-friendly hierarchically porous architectured carbon electrode and flexible biopolymer electrolytes are employed as significant components in a coin cell-based all-solid-state supercapacitor. The resulting device delivers a high specific capacitance of 240 Fg^{-1} at 0.5 mA with 97% coulombic efficiency over 2000 cycles. In addition, the device provided excellent specific energy (17 Wh kg^{-1}) and specific power (3823 W kg^{-1}). Interestingly, the starch derived biopolymer electrolyte film, when buried under soil, shows a favourable natural rate of degradation. Therefore, this fabricated electric double layer capacitor can be used as a promising device with little to no potential environmental harm.

1. Introduction

Electric double layer capacitors (EDLCs) have captured attention due to their high-power density and rapid charge/discharge rates without compromising its cycling stability [1]. EDLCs store energy electrostatically between the electrode/electrolyte interfaces at the

* Corresponding author.
E-mail address: selvankram@buc.edu.in (R. Kalai Selvan).

https://doi.org/10.1016/j.jcis.2019.06.081
0021-9797/

high surface area of working electrodes [2–4]. Based on the energy storage mechanism, the density of stored energy in EDLCs relies solely on the surface chemical properties of the electrode material. As far as EDLCs are concerned, a carbon electrode favours ionic transportation, which boosts adsorption/desorption, enhances conductivity and stays resistant to corrosion [5–7]. In this regard, eco-friendly hierarchical porous activated carbon (HPAC) based electrodes sequestered out of bio-waste materials have received considerable attention due to its high specific surface area, porous architecture and organized with electro-active organic functional groups [6]. These carbon materials are obtained from bio-waste materials through conventional methods such as physical activation, chemical activation, and hydrothermal methods [7–13].

Among different biomasses [14–18], the chemical structure and abundance of starch $(C_6H_{10}O_5)_n$ are favourable features for precursors to HPAC materials. Starch polysaccharide granules are comprised of two types of molecules; branched amylopectin (usually 70–80%) having $\alpha(1 \rightarrow 4)$, $\alpha(1 \rightarrow 6)$ glycosidic linkages, and helical amylose (usually 20–30%) having α $(1 \rightarrow 4)$ glycosidic linkages containing 49% of oxygen. While burning off, the surface —OH groups get removed, and activated carbon (AC) materials with high surface area and extreme porosity will be obtained [15]. In recent decades, potato starch [7], commercial soluble starch [9], sweet potato starch [14], and cellulose starch [16] have been used as precursors to derive porous carbon in EDLCs applications. Apart from high surface area and organic functional groups, the addition of heteroatoms can further improve the specific capacitance (C_{sp}) of EDLCs [17].

Herein, *Artocarpus heterophyllus* seed (AHS) is selected as the source for the preparation of starch since it contains a rich source of vitamin, minerals, phytonutrients, starch, electrolytes, fibre, fat and protein as shown in Fig. S1 [18–19]. The starch and phytonutrients in its nutshell deliver HPAC with high surface area and heteroatom organization. To the best of our knowledge, this is the first reported work on the use of starch derived from AHS for the preparation of carbon as supercapacitor electrodes. However, the preparation of HPAC directly from AHS seed powder has been reported; Khairnar et al. [18] designed a carbon material with a surface area of 114 $m^2 g^{-1}$ which delivered a specific capacitance of 92 Fg^{-1} while Kalyani et al. [20], prepared hetero-atom inbuilt activated carbon with a surface area of 932 $m^2 g^{-1}$ and attained a specific capacitance of 203 Fg^{-1} with AHS precursor. Refining and tuning the chemical structure of AHS is expected to deliver a high surface area AC electrode with inbuilt heteroatoms and improved capacitive performance.

On the other hand, electrolyte also plays a crucial role in determining the overall performance of EDLCs. Safety concerns, lack of portability and the narrow potential window of aqueous electrolytes have given rise to the need for alternatives. In this regard, biopolymer electrolytes have captured research interest [21–22] due to their widespread availability, versatility, low cost, excellent mechanical and electrical properties, and ease of manufacture. Besides, these biopolymers have no toxic residues and potentially enrich the quality of soil during degradation. Till now, biopolymers have been prepared from starch, cellulose, gelatin, chitosan, and lignin, which are biodegradable and compostable [22–27]. In this study, starch is chosen as the starting material to build the biopolymer electrolytic film (BPEF). Many starch-based biopolymers electrolytes have been reported in recent years, including corn starch with lithium acetate (LiAc) [24], chitosan and Li^+/Ag^+ [25], cellulose acetate (CA) with varying concentrations of $LiClO_4$ [27], and a starch-chitosan blend with NH_4Br [29]. In this report, *Manihot Esculenta* starch (MES) without any ionic liquid additive is employed to prepare a biopolymer electrolyte film for an all-solid-state supercapacitor. MES contains 80% carbohydrate, which is renewable and is available in many parts of the world. Juan Zeng et al., recently reported an all-solid-state supercapacitor with all key components (electrolyte, separator, binder, and electrodes) entirely from a single kelp precursor. The all-solid-state supercapacitor delivered a high specific capacitance of 227 Fg^{-1} utilizing the high surface area carbon (4425 $m^2 g^{-1}$) sequestered from kelp with a high pore volume up to 3.22 $cm^3 g^{-1}$ [28]. The above report stimulated the concept of using starch as a starting material for the preparation of a bio-degradable electrode and polymer electrolyte film.

In this work, a bio-degradable AC electrode having a higher specific surface area and hierarchical porous architecture is developed through a single-step $ZnCl_2$ activation process. Subsequently, a biopolymer electrolyte film is also prepared from MES powder using an eco-friendly solvent casting process under ambient atmosphere. With the as-prepared AC electrode and MESF electrolyte, the symmetric coin cell-based all-solid-state high-performance EDLC is fabricated. The combination attained a maximum specific capacitance, high specific energy, high specific power and excellent cyclic stability.

2. Experimental methods and materials

2.1. Materials and source purity

Materials, fresh *Artocarpus heterophyllus seeds* and *Manihot esculenta* were obtained from the local market (Coimbatore, Tamilnadu, India). Zinc Chloride ($ZnCl_2$, High media chemicals, AR grade) was used as a chemical activation agent without any further purification. Double distilled (D-D) water was used to prepare solutions and wash samples. High pure sulphuric acid (H_2SO_4, 95.0–98.0%, Sigma Aldrich chemicals, AR grade), Sodium hydroxide (NaOH, High media chemicals, AR grade) and Glycerin ($C_3H_8O_3$, High media chemicals, AR grade) were used as received without any purification.

2.2. Starch extraction from Artocarpus heterophyllus seeds (AHS)

For the preparation of a biomass-derived electrode, the AHS was used as a source for deriving starch, and a step by step procedure is given in Fig. 1. Initially, AHS (500 g) was separated from the fleshy fruit, white and brown carpels were peeled off, and waxy, wet seeds were obtained. The wet seeds were washed with double distilled (D-D) water and followed by ethanol several times. Once cleansing was complete, the seeds were mechanically ground with D-D water to obtain a colloidal suspension. The solution was filtered using a sieve to reduce the particle size, and the starch particles were allowed to settle for 30 min. This step was repeated until a clear solution was obtained. The creamy, foam layer of starch particles was collected while the solution was poured off. A pale-yellow aromatic wet flour-like substance was obtained, which was dried at 80 °C for 12 h to remove moisture. The final foamy starch powder was collected, weighed and placed in an air-tight jar.

2.3. Activated carbon sequestration from AHS starch

The detailed procedure for the sequestration of activated carbon from AHS starch is also shown in Fig. 1. For the typical preparation, two grams of starch powder was mixed with 10 mL of D-D water containing 2 g of $ZnCl_2$, giving an impregnation ratio (IR) of 1: 1 (starch:$ZnCl_2$), was magnetically stirred for 12 h and followed by 2 h under bath sonication. Then the composites were oven dried for 12 h at 120 °C to obtain a carbo-crisp. Subsequently, the porous carbo-crisp was chemically activated for 3 h at 700 °C under constant N_2 flow in a tubular furnace. The obtained carbon sample

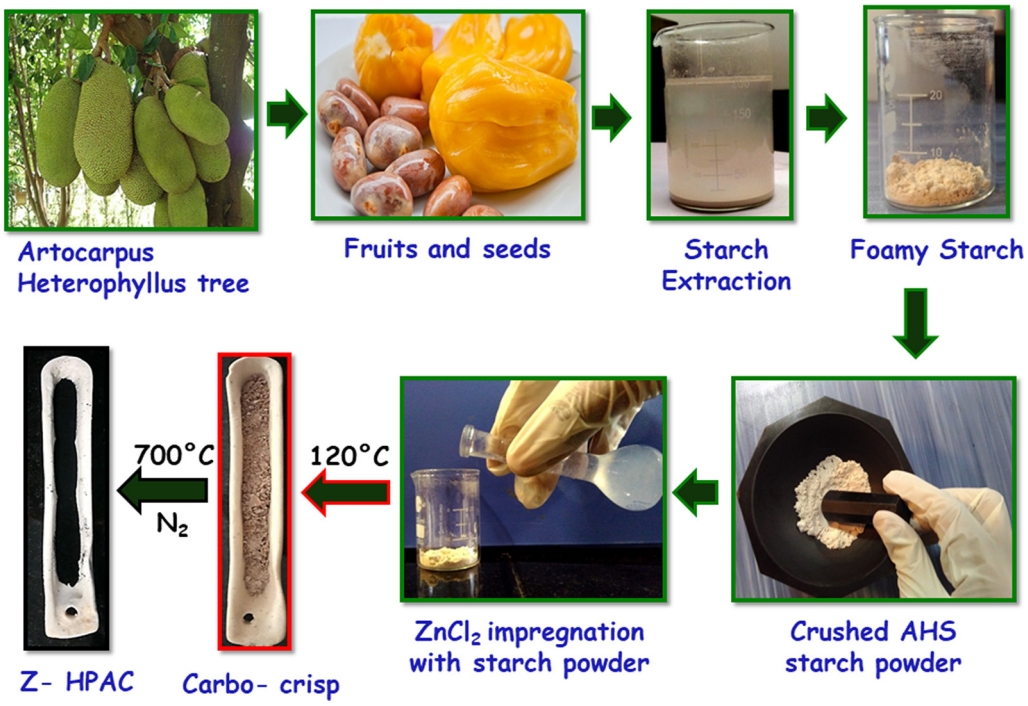

Fig. 1. Pictorial representation of the preparation of foamy starch powder from Artocarpus heterophyllus seed (AHS) and activated carbon (AC) through the chemical activation process.

was soaked in 0.1 M of HCl and washed with D-D water and ethanol to remove chloride impurities. The washing was continued until the carbon-containing solution reached pH 7 with Whatman® indicator papers (standard full range, 1.0 to 14.0). Finally, the solution was left to dry in an oven at 80 °C overnight to obtain HPAC materials. Starch/$ZnCl_2$ with different IR of 1:2 and 1: 3 were similarly prepared to obtain other HPAC (Z-HPAC) materials. Samples with IR 1:1, 1:2 and 1:3 were labelled as Z1, Z2, and Z3, respectively and collectively referred to as Z-HPAC materials. The yield percentage of Z-HPAC was calculated by taking the final mass of AC material divided by the initial mass of crushed carbo-crisp before activation by the following equation [29],

$$Yield(\%) = \frac{w_f}{w_i} \times 100 \quad (1)$$

where, w_f and w_i are the final weight of AC (g) and the initial weight of the of dried carbo- crisp (g).

2.4. Preparation of flexible Manihot esculenta starch film

The highly flexible *Manihot Esculenta starch* film (MESF) was prepared via a conventional solvent casting process, as shown in Fig. 2(a–f). Initially, one gram of cassava starch was dissolved in 15 g of D-D water and stirred until it turned a milky white (Fig. 2b). Concurrently (Fig. 2c), 0.5 mL of glycerine, 0.2 mL of 1 M H_2SO_4 and 0.5 mL of 0.1 M NaOH (to attain pH 7) was added to the above suspension at ambient temperature. Details of the experimental optimization of plasticizer and support electrolytes are given in Table S1. Then the mixed solution was heated around 50 °C. During heating, the gradual transformation of the milky solution into a transparent gel-like suspension was observed within seconds (Fig. 2d). Temperature and stirring rate were set to 50 °C and 150 rpm, respectively, to maintain the consistency of the gelation process. After 15 s, approximately 20 mL of transparent, odourless solution was obtained. The obtained gelatinous specimen was immediately cast on to a polypropylene petri dish (Fig. 2(e and f)) and left undisturbed for 24 h in the open air to allow the formation of transparent, flexible and bubble free *Manihot Esculenta* starch film (MESF), (Fig. 2g). The MESF was carefully peeled off from the petri dish using smooth forceps. The mechanical flexibility of MESF in different orientations is shown in Fig. 2(h and i). Details of electrode preparation, device fabrication, material characterization and electrochemical measurements are provided in the electronic supplementary information (ESI).

2.5. Bio-degradability test of MESF

Bio-degradability test of MESF was performed with 100 g of sandy clay loam collected from Coimbatore, Tamil Nadu. Before burying MESF into the soil, the soil properties were determined. The collected reddish-brown soil had a high degree of calcareous content within its matrix. The pH of the soil was 8.31, and it exhibited an electrical conductivity of 0.91 ds m^{-1} (non-saline). Nitrogen (N), phosphorous (P) and potassium (K) content of the soil was approximately 210 kg ha^{-1}, 27 kg ha^{-1}, 441 kg ha^{-1}, respectively. After burying MESF under the soil, the film was rinsed thoroughly using D-D water and dried in the ambient atmosphere. The weight loss percentage is calculated from the following equation,

$$Weight\ Loss(\%) = \frac{W_i - W_f}{W_i} \times 100 \quad (2)$$

where W_i is the initial weight of the MESF and W_f is the weight of the MESF after burial test. Initially, the MESF weighed about 13.69 mg, the film was directly buried under the sandy clay loam. The percentage of weight loss was calculated every 24 h, and it was left to degrade for about 40 days. Besides, the detailed description on electrode preparation, device fabrication, material characterization and electrochemical measurements are provided in the electronic supplementary information (ESI).

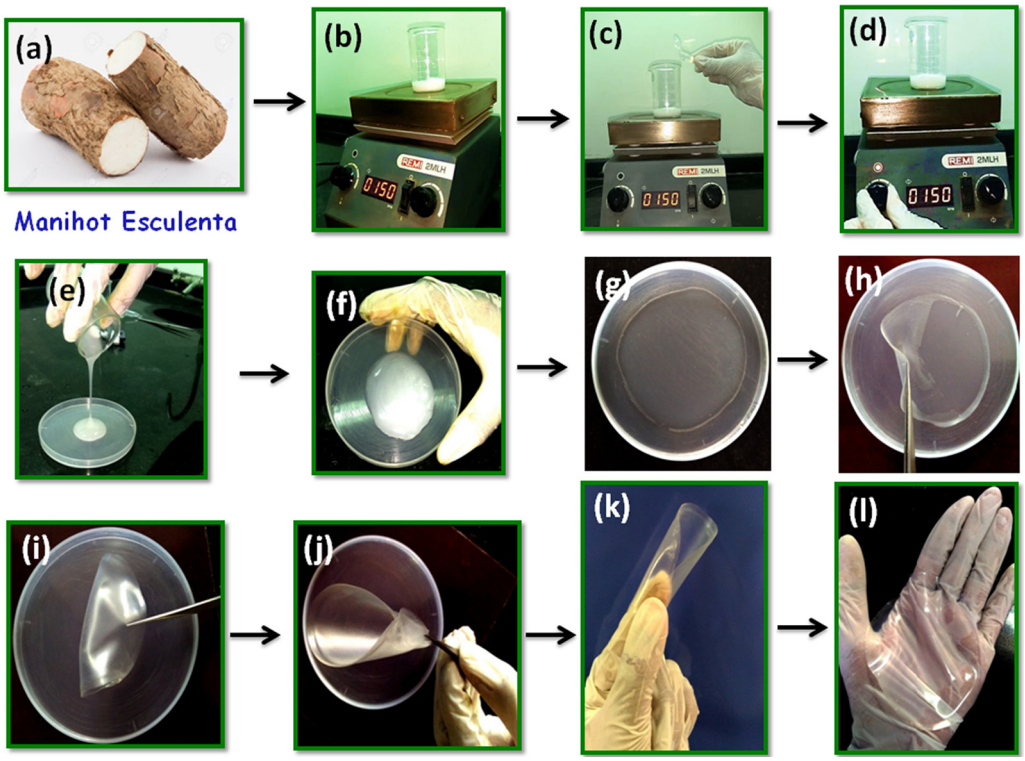

Fig. 2. (a–l). Pictorial representation of the preparation of biopolymer electrolyte from Manihot Esculenta.

3. Results and discussion

3.1. The physicochemical properties of hierarchically porous activated carbon (Z-HPAC).

3.1.1. Structural properties

The XRD patterns of Z-HPAC materials are shown in Fig. 3a. All the patterns exhibited two broad XRD peaks in between 22 & 30° and 42 & 45°, corresponding to the (0 0 2) and (1 0 0) planes respectively, and matched with the JCPDS (card No. 89-8487) of graphitic carbon [30]. The broad hump (0 0 2) occurs due to the irregular arrangement of aromatic sheets and aliphatic side chains attached to the carbon matrix due to high-temperature carbonization [31]. Similarly the (1 0 0) diffraction plane arises due to interlayer condensation of graphite. Table 1 indicates that while increasing the impregnation ratio, the broadness of the (0 0 2)

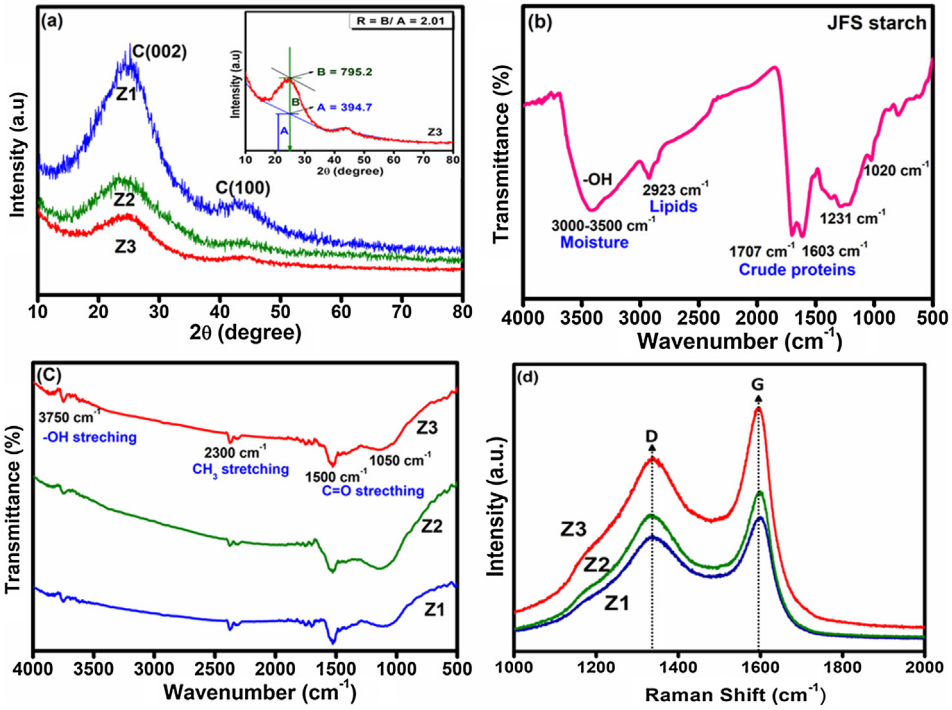

Fig. 3. (a) XRD patterns (inset:R factor calculation), (b) FTIR spectrum of AHS starch, (c) FTIR spectra of Z-HPAC samples and d) Raman spectra of Z-HPAC samples.

Table 1
Structural parameters of the prepared ACs obtained from XRD pattern.

Sample	IR	% of yield	β	d_{002}	R	L_a (Å)	L_c (Å)	N (Å)	n
Z1	1: 1	76.03	0.24	0.367	1.3	12	5.8	2.5	2.1
Z2	2: 1	80.12	0.20	0.364	1.4	14	6.9	2.9	2.7
Z3	3: 1	82.06	0.18	0.359	1.5	16	7.8	3.2	3.3

IR: Impregnation Ratio, **R:** Residual factor, L_a: Size of the large plane, L_c: Crystallite size along the c-axis, **N**: number of layers, **n:** Average number of carbon atoms per aromatic lamellae

plane widens, whereas the intensity of the (1 0 0) plane decreases in the order of Z3 > Z2 > Z1, suggesting that the carbon network becomes more disordered. The obtained d-spacing (d_{002} > 0.334 nm) (Table 1) reveals a turbostratic or random layer lattice structure of the prepared HPAC materials [28,32] that likely enhances ionic and electrical conductivity during the electrochemical process [34]. The calculated residual factor or R-factor (i.e. the ratio of the height of the (0 0 2) peak with respect to the background) is proportional to the concentration of single and multi-layered aromatic sheets aligned at the corner in a non-planar format. Here, the R-factor (inset: Fig. 3a) is high for Z3 (1.5), suggesting a disruption of the carbon skeleton and creation of more active sites at the edges due to the $ZnCl_2$ activation [33]. Further, the calculated size of the large plane (L_a = 1.84 λ/β Cos θ, Å), crystallite size along the c-axis (L_c = 0.89 λ/β Cosθ, Å), number of layers ($N = (L_c + d_{002})/d_{002}$) and average number of carbon atoms per aromatic lamellae ($n = 0.32\ N^2$) are given in Table 1. It reveals that the percentage of carbon atoms and the degree of parallel stacking is greater in Z3 than the Z1 and Z2 materials [34].

Fig. 3(b, c) shows the FTIR spectra of the prepared starch powder and Z-HPAC materials, respectively. The FTIR spectrum of AHS derived starch (Fig. 3b) contains moisture, lipid molecules, crude protein, amylose and amylopectin with the emergence of –OH stretching (3500–3000 cm^{-1}), CH_2 asymmetric stretching (2850–2930 cm^{-1}), C═O stretching (1600–1700 cm^{-1}), —CHOH stretching (1200–1300 cm^{-1}) and C—O—C bending (790 and 608 cm^{-1}), respectively [35]. After high-temperature carbonization at 700 °C (Z-HPAC), the thermally unstable moisture content, lipid molecules and acidic oxides (carboxylic, anhydrides, hydroxyls) on the surface of the starch sample are lost (Fig. 3c). It is observed that the effect of impregnation ratio and activation temperature caused shifts and loss of bands in the FTIR spectra of Z1, Z2, and Z3. Shifts in the –OH absorption band from 3500 cm^{-1} to 3752 cm^{-1} can be accounted for evaporation of naturally occurring water molecules during pyrolysis [36]. Moreover, neutral surface oxides (CH_3 stretching) and unsaturated sites are found around 2300–2380 cm^{-1}. The bumpy absorption bands around 1500–1700 cm^{-1} are associated with nitrogen functionalities and a carbonyl group (aromatic structure). A small cliff observed in 1574 cm^{-1} suggest the presence of nitrogen species group attached to the carbon surface as a result of high temperature (>600 °C) [37]. A mild absorption band correctly centred at 1300–800 cm^{-1} results from C—O stretching and O—H bending vibrations of carbonyl, alcohol, and phenol groups present in the starch molecules [9]. It is clear from the FTIR spectra that oxygen and nitrogen functional species are the major components of the surface of Z-HPAC materials. These functional species are expected to serve as active sites on the conductive carbon surface to adsorb more ions from the electrolyte during redox activity and enhance the overall performance of EDLC [7].

Raman spectra (Fig. 3d) reveal the graphitization quality of the Z-HPAC materials. All the Z-HPAC materials exhibit two characteristic peaks; a D-band (near 1336 cm^{-1}) and G-band (near 1596 cm^{-1}), representing the disordered and graphitic nature respectively [38]. The graphitic band is closely associated with the vibrations of sp^2-bonded carbon atoms in the 2d hexagonal lattice, while the defect peak arises due to sp^3-hybridized carbon. These findings confirm a turbostratic structure [11]. The graphitization degrees (I_D:I_G) reveal higher electrical conductivity for Z3 (0.79) compared to Z1 (0.859) and Z2 (0.850). The in-plane graphitic crystallite size (L_a) is determined using the Tuinstra–Koenig equation, [39]

$$L_a(nm) = \left(2.4 \times 10^{-10}\right) \lambda_l^4 \left(\frac{I_D}{I_G}\right)^{-1} \quad (3)$$

where λ_l is the laser line wavelength. Calculated L_a for Z1, Z2, and Z3 is 3.8, 3.7 and 3.4 nm, respectively, in concord with the XRD results. Hence, the Z-HPAC materials with inbuilt heteroatomic functional elements possess a disordered turbostratic structure, particularly Z3.

To determine the elemental occurrence on the surface of the Z-HPAC samples, X-ray photoelectron spectroscopy (XPS) was performed (Fig. 4). The peaks found at 283.7 eV, 532.8 eV and 400.9 eV in the survey spectra (Fig. 4a) confirm the presence of C, O, and N, respectively [39]. Fig. 4(b–d) shows the high-resolution deconvoluted spectra of C1s, O1s and an N1s peak of the Z3 material. The carbon trace found at 283 eV for Z3 (Fig. 4(b)), is deconvoluted into three major peaks which relate to C—C (284.6 eV), C—N (amine) or C-OH (hydroxyl) or C—O—C (ether) (286.4 eV), and C═O (methyl or ethyl group) (289.3 eV) [23]. The complete transformation of ordered and amorphous crystalline lamellae of amylose and amylopectin organic polymer into turbostratic carbon with sp^2 hybridization is evidenced through the high-intensity peak at 284.6 eV. The other two moderate peaks at 286.4 and 289.3 eV confirm the involvement of oxygen and nitrogen functional groups on the surface of the carbon [12,40]. Fig. 4(c) shows four deconvoluted peaks of oxygen at 530.7, 531.14, 532.8 and 535.4 eV. These peaks confirm that the involvement of oxygen is not only due to the presence of inbuilt oxygen species on the carbon surface but also due to the adsorbed oxygen ions in the deficient regions. Each peak is related to the irreversible adsorption of neutral oxides (>C═C <) present in the starchy component [36]. Co-ordination of oxygen species on the carbon surface depends on the parameters involved in chemical activation [17]. The N1s spectrum of Z3 material is deconvoluted into two peaks (Fig. 4d). The deconvoluted N1s spectrum is found with pyrrolic (at 401.6 eV) and pyridinic (at 398.4 eV) type nitrogen species, inherited within the carbon matrix as a result of protein content in the nutshell of AHS starch. In particular, pyrrolic N has five valence electrons, and sp^3 hybridized and hence shares one or two electrons with the aromatic carbon and hydrogen via σ bonding, with a bond length of 137 pm. While Pyridinic N is sp^2 hybridized and shares two electrons with the carbon atoms at the edges through π bonding with a bond length of 115 pm [41–42]. It is clear that structural deformation occurring on the carbon surface during pyrolysis is due to the inherited *N*-atoms within the carbon matrix. The existence of a high atomic percentage of nitrogen functionalities (2.1 at. wt.%) on carbon even after high-temperature carbonization suggests that pyrrolic and pyridinic type nitrogen is independent of temperature. Also, the low surface oxides found on the Z3 carbon surface are the reason for the attachment of an increased number of nitrogen-

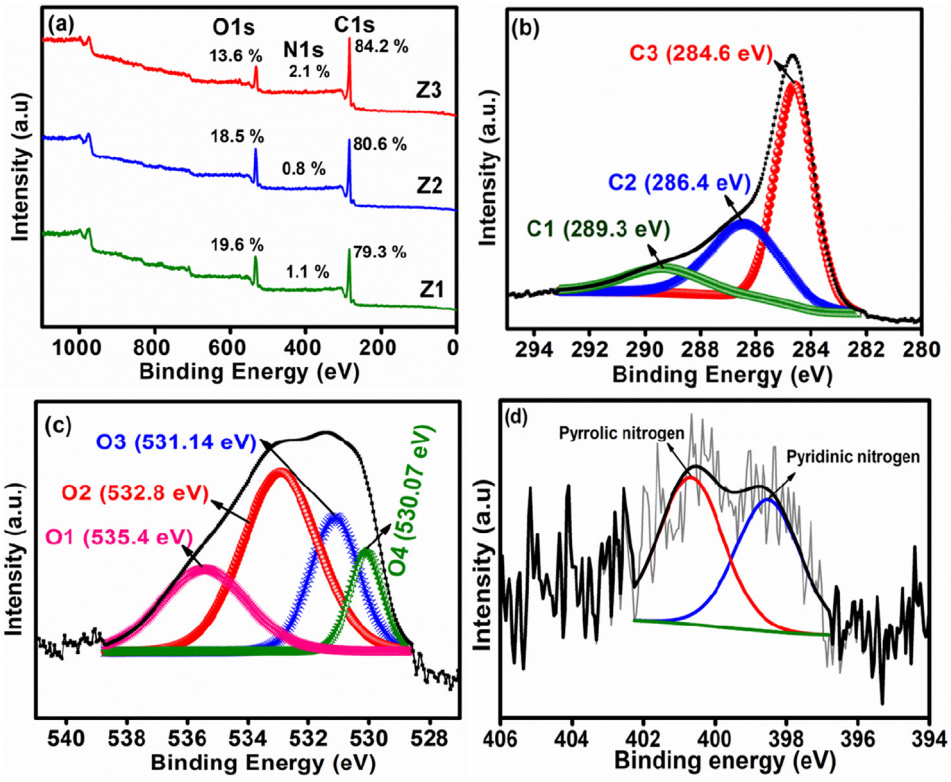

Fig. 4. (a) XPS Survey spectra of Z-HPAC and high-resolution XPS spectra of deconvoluted b) C1s peak, (c) O1s peak and (d) N1s peak of Z3 material.

containing functional groups after pyrolysis. These type of nitrogen species are the cause of structural and electronic changes and serves as a permeable medium for the mobility of ions during the redox reaction [38 –39]. Fig. S2 (a-f) shows the high-resolution deconvoluted spectra of C1s, O1s and N1s peak corresponding to Z1 and Z2 samples, respectively. Table 2 shows the ratio of total oxygen to carbon content (O/C) and total nitrogen to carbon content (N/C) of Z-HPAC materials. It can be seen that Z3 has a lower degree of surface oxidation and a high amount of nitrogen functionalities relative to Z1 and Z2. Therefore, Z3 is expected to provide higher electrical conductivity due to the existence of rich carbon trace while the surface nitrogen functionalities on its surface contribute to wettability and serve as a support to adsorb ions during charge storage.

3.1.2. The textural and morphological properties

Fig. 5(a–c) shows the N_2 adsorption/desorption isotherms of Z-HPAC materials. The materials exhibit mixed isotherm characteristics (i.e., isotherms I and IV as per IUPAC classification) [8]. The vertical rise with no hysteresis loop in the N_2 adsorption-desorption isotherm under relatively low pressure ($P/P_0 < 0.01$) reveals the existence of the micropore network. The observed hysteresis loop ($0.45 \leq P/P_0 < 0.9$) confirms the presence of mesopores with uniform size distribution [6]. Amongst the prepared Z-HPAC samples, Z3 shows a gradual broadening in the hysteresis loop (Fig. 5(c)), suggesting the existence of more mesoporous network due to the optimal impregnation ratio and acid etching during the wash. Table 2 shows that the Z3 sample has a high surface area (1841 m^2/g), mean pore diameter (2.6 nm), micropore volume (1.18 cm^3/g) and average pore size (1.2 nm) compared to the other two materials. Similarly, the specific surface area of Z3 is superior to those of recently reported $ZnCl_2$ impregnated biomass-derived AC, such as $ZnCl_2$/*liquefied wood* (1423 $m^2\ g^{-1}$) [33], $ZnCl_2$/*date seeds* (1050.01 $m^2\ g^{-1}$) [36], $ZnCl_2$/*pteroceltis tatarinowii maxim* bark (1210 $m^2\ g^{-1}$) [43], $ZnCl_2$/*peanut shell* (1549 $m^2\ g^{-1}$) [44], $ZnCl_2$/*pine cone* (1839 $m^2\ g^{-1}$) [45], $ZnCl_2$/*bradyrhizobium japonicum* (1275 $m^2\ g^{-1}$) [46], and $ZnCl_2$/*palm kernel shell* (1058 $m^2\ g^{-1}$) [47]. In the context of supercapacitor electrode, Z3 material containing high surface area sculptured with hierarchical porous architecture is expected to play an important role in the chemisorption, electrostatic interactions, and ionic transportation process [11].

The morphology of Z-HPAC is revealed through FE-SEM images (Fig. 6(a–c)). The overall FE-SEM images of Z-HPAC materials appear to seem like some irregular shaped druse and geodes of different sizes being placed randomly on a rough platform. The formation of high surface carbon and the opening of the porous network are depicted through schematic representation (Fig. 6d). Further, the Z3 material is characterized using TEM (Fig. 7(a)) and HRTEM (Fig. 7(b and c)) analysis. The TEM and HRTEM images display the porosity (with a wide distribution of defined pores) and tight ring-shaped carbon layers, in concord with the d-spacing

Table 2
Parameters calculated from XPS and BET analysis.

Sample Name	N/C	O/C	a_s, BET (m^2/g)	Mean pore diameter (nm)	Total micropore volume (cm^3/g)	Pore Size (nm)
Z1	0.014	0.24	1472	1.8	0.65	0.7
Z2	0.009	0.23	1746	2.3	1.03	1.1
Z3	0.024	0.16	1841	2.6	1.18	1.2

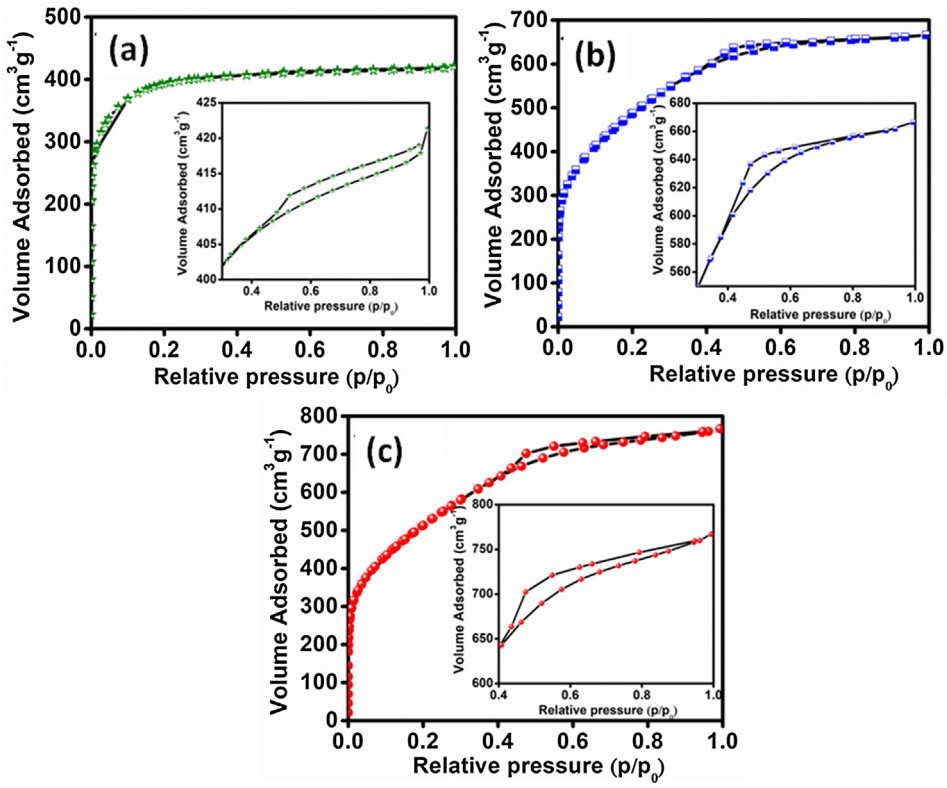

Fig. 5. Nitrogen adsorption/desorption isotherms of activated carbon materials (a) Z1, (b) Z2, and (c) Z3 samples.

(0.354) of 002 planes of XRD pattern (Fig. 3a). Further, the SAED (Fig. 7d) pattern elucidates the amorphous nature of prepared activated carbon. The presence of heteroatom is confirmed through FESEM-EDX (electron dispersive X-ray spectroscopy) elemental mapping (Fig.S3). This EDX mapping illustrates the widespread distribution of C (93.2%) and sparse presence of N (2.99%) and O (3.75%) in comparison, thereby qualitatively confirming the XPS analytical findings.

Further, to investigate the wettability of the materials, the contact angle (CA) measurement was performed. Fig. 8 shows the rep-

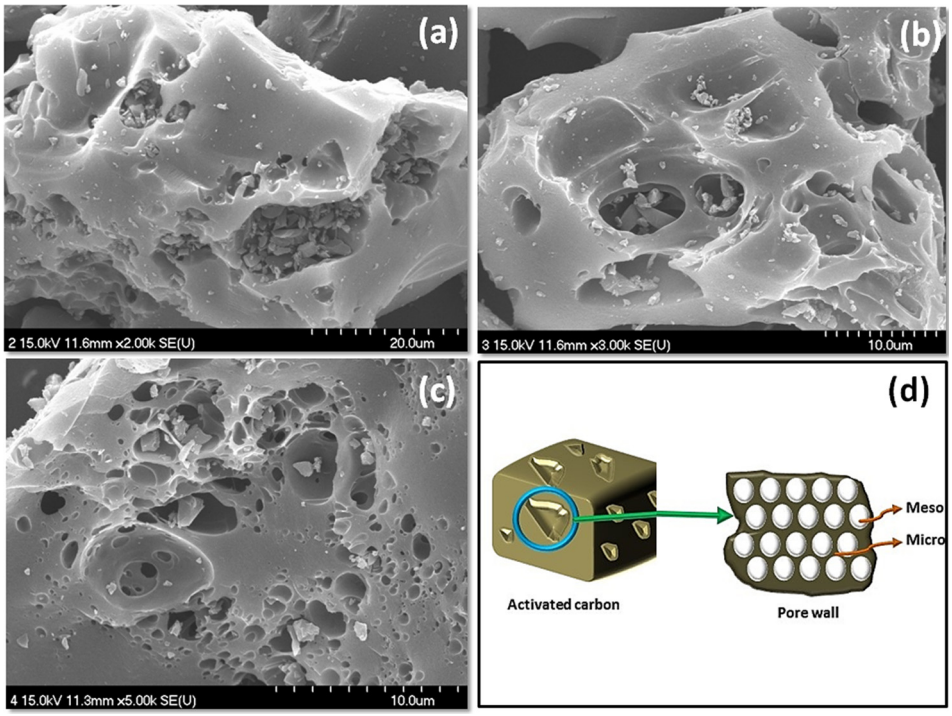

Fig. 6. FESEM images of (a) Z1, (b) Z2 and (c) Z3 activated carbon materials. (d) Schematic representation of porous architecture in the Z-3 materials.

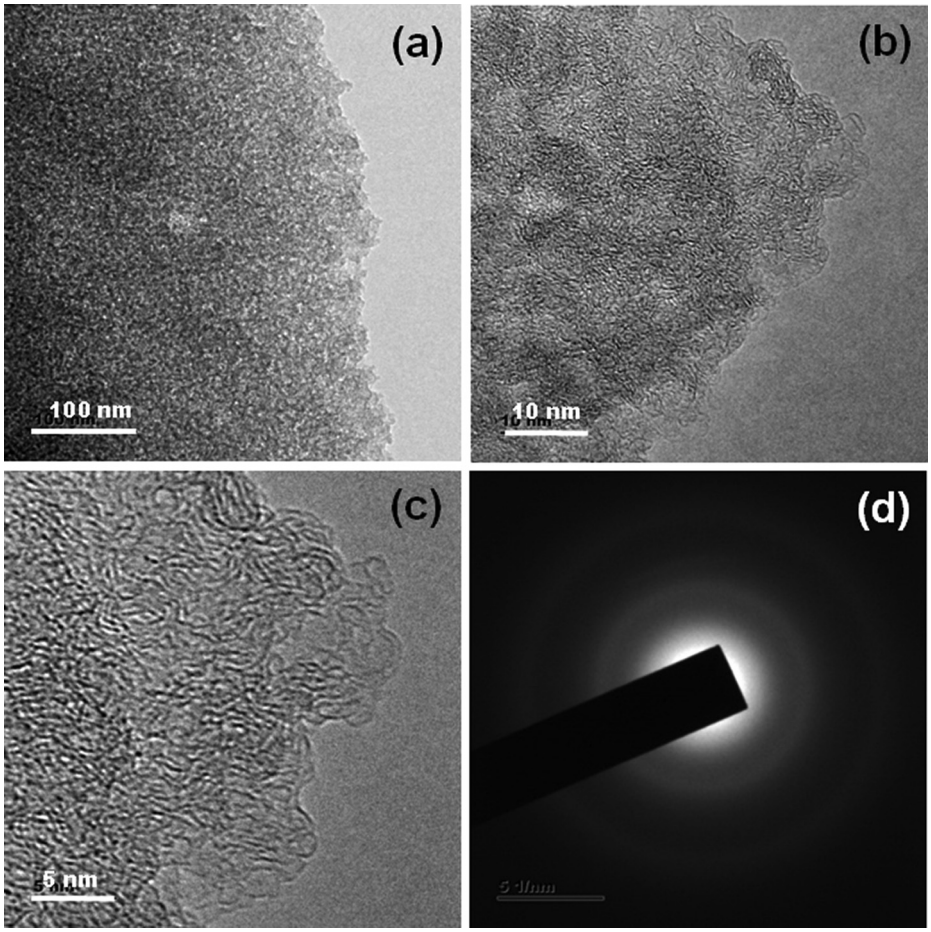

Fig. 7. Representation of (a–c) TEM and HRTEM images, (d) SAED pattern of Z3 activated carbon.

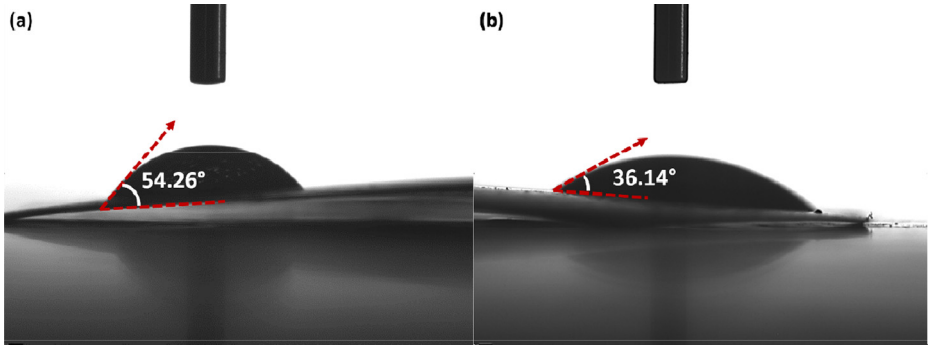

Fig. 8. Contact angle measurement of Z3 electrodes in (a) H_2O and (b) H_2SO_4 electrolytes.

resentative contact angle measurement of the Z3 sample measured in two different electrolyte mediums of H_2O (Fig. 8a) and H_2SO_4 (Fig. 8b). It can be seen that the contact angle in 1 M H_2SO_4 is 36.14°, which is very low when compared with H_2O medium (54.26°). It infers that the Z3 electrode is highly hydrophilic in H_2SO_4 electrolyte. Hence, the electrolyte ions can easily penetrate and facilitate through the porous architecture of activated carbon [11–12]. Therefore, 1 M H_2SO_4 would be a promising supporting electrolyte for improvising the electrochemical performance of Z3-SC device. Overall, it is clear from the above discussion that Z3 has a high degree of graphiticity, high surface area (1841 $m^2\ g^{-1}$) and average pore size (2.6 nm), high amount of nitrogen species (2.1 at. wt %) and organic (carboxyl and oxygen) functional groups organized on its surface. Therefore, these porous networks do not serve only as reservoirs for accumulation electrolytic ions but also involves in the rapid transportation of ionic species from the electrolytic medium to the inner pores on the electrode surface during redox process [43,47]. Hence, it is believed that it can provide an excellent specific capacitance and rate capability for the supercapacitor applications.

3.2. Physicochemical properties of Manihot esculenta starch film (MESF) as electrolyte

Fig. 9 (a) shows the FTIR spectrum of *Manihot esculenta* starch derived flexible biopolymer electrolytes to determine the func-

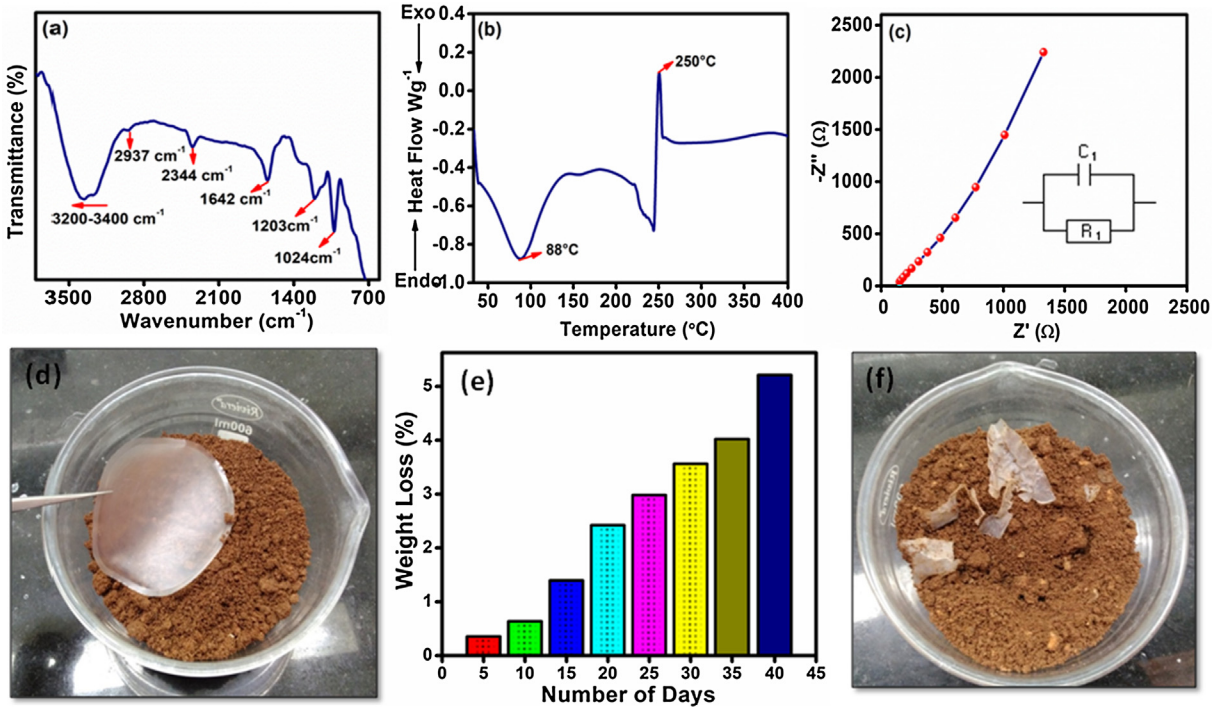

Fig. 9. (a) FTIR spectrum, (b) DSC analysis, (c) Cole-Cole plot of MESF biopolymer. (d) Initial Exposure of MESF to sandy loam clay, (e) weight loss% of MESF (40 days) and (f) Appearance of MESF after Soil- burial test.

tional groups present in the film. The observed bands at 3200-3400, 2937, 2344, 1642, 1203 and 1024 cm^{-1}, represent the respective functionalities present in the MESF. The band observed at 3200–3400 cm^{-1} corresponding to the –OH stretching vibration, which, is due to the starch solvation with a rise in temperature [48,49]. Due to the hydrophilic nature of Cassava starch, the C-H_2 asymmetric stretching vibrations of aliphatic groups and protein molecules, C-OH stretching of glycerol, C—O stretching of alcohol and antisymmetric stretching of C—O—C are also found in the FTIR spectrum of *MESF* [48,50]. The obtained MESF is highly moist and functionally organized, which is expected to yield higher conductivity and serves as a porous medium for accessing ionic species during the EDLC mechanism [51]. It is essential to understand the temperature effect of MESF plasticization, Fig. 9(b) shows the DSC curve of MESF measured in the temperature range 40–400 °C. The temperature at which the semi-crystalline granules are transformed into a homogeneous, transparent, viscous gel is the glass transition temperature (T_g). The plot shows a strong endothermic peak at 65 °C (the melting point of MESF), at which the solvated transparent liquid converted into viscous polymeric gel electrolyte. The observed T_g is low because the gelation mechanism breaks down hydroxyl functional groups and creates a new bonding with the glycerine molecules [51]. Hence, the amount of water molecules and the plasticizing agent determines the melting temperature of the polymer. Lu et al. reported that T_g between 60 and 80 °C is absolute to obtain thermoplastic membrane in the presence of water [52]. The lowest T_g value infers that glycerine is the most efficient plasticiser to modify starch into biopolymer electrolyte film compared to the other systems, as it has more —OH groups than the rest that improve the plasticization and absorb the ion conducting H_2SO_4 molecules into its network. Hence, the enhanced structural stability helps in sustained ionic charge mobility during electrochemical redox activity. Also, the measure of conductivity is an important parameter to be evaluated before the fabrication of coin cell supercapacitor.

Fig. 9(c) shows the Cole-Cole plot of the prepared MESF and its corresponding equivalent circuit is given in the inset (Fig. 9c). In general, the Cole-Cole plot is a combination of semicircle attached with a spike at an angle of <90° with respect to the X-axis. Here, the pure MESF exhibits a non-vertical spike at the low-frequency region due to the polarization effect at the electrode/electrolyte interface due to capacitor effect. The semi-circle in the high-frequency region is absent; only the resistive component is active in the MESF. The prepared MESF has a bulk resistance of 6.45 Ω. Therefore, the calculated conductivity of MESF is 3.1×10^{-3} S cm^{-1}, using the following equation [53],

$$\sigma = \frac{l}{R_b A} \tag{4}$$

where l is thickness, A is an area, and R_b is the bulk resistance of the electrolyte film. The obtained conductivity of MESF is higher than ternary natural deep eutectic solvent (NADES) infused *Phthaloyl* Starch (2.86×10^{-3} S cm^{-1}) [22], glycerol incorporated *potato starch* (1.3×10^{-5} S cm^{-1}) [51], 1-methyl-3-propylimidazolium iodide ionic liquid added *rice starch* and (1.20×10^{-3} S cm^{-1}) [53], starch–chitosan blend (5.1×10^{-4} S cm^{-1}) [54], NH_4Br-doped corn-starch (1.8×10^{-3} S cm^{-1}) [55], Silver ion (Ag) doped Starch (1.03×10^{-9} S cm^{-1}) [56], *sago (Metroxylon sagu)* starch (3.69×10^{-4} S cm^{-1}) [57], potassium iodide (KI) and iodine added *sago palm* starch (3.4×10^{-4} S cm^{-1}) [58], based biopolymer electrolyte film. Therefore, the present case obtained high conductivity infers that MESF holds many mobile charge carriers within its amorphous polymer matrix.

As an environmental concern, the biopolymer electrolyte film is subjected to a soil bio-degradability test for about 45 days, to ascertain the nature and rate of its decay (Fig. 9(d–f)). The percentage of weight loss of MESF with time is plotted as a bar graph in Fig. 9(e). It can be observed that the film showed a rapid decay of 0.35% during the initial period and started to decay gradually and reached a degradation order of about 5.2% at the end of the

40th day as shown in Fig. 9(f). The soil properties and chemical composition of MESF are the main factors that determine the rate and degree of bio-degradation of MESF matrices. The MESF buried under alkaline rich soil undergoes weight loss due to the bio-degradation process. The micro-organisms present in the soil gradually spread and covers the entire surface of MESF and eats the polysaccharides, due to which the decay and weight loss occur [24,59]. The result suggests that the synthesized MESF biopolymer electrolyte film is eco-friendly.

3.3. Electrochemical performances of all-solid-state fabricated EDLCs

To evaluate the electrochemical performances of the fabricated all-solid-state supercapacitor using biomass-derived electrodes (Z-HPAC) and *Manihot esculenta* starch film (MESF), the cyclic voltammetry (CV), charge-discharge measurements (GCD) and electrochemical impedance spectroscopy (EIS) analysis are carried out. The symmetric configurations of the solid-state supercapacitors are Z1||MESF||Z1, Z2||MESF||Z2 and Z3||MESF||Z3 named hereafter Z1-SC, Z2-SC, and Z3-SC, respectively. Fig. 10a represents the CV performance of all the devices at a sweep rate of 2 mV s^{-1}. For qualitative explanation, the specific capacitance (C_{sp}) is calculated for the three supercapacitors (equation S1), revealing Z3-SC supercapacitor exhibiting highest specific capacitance (C_{sp}) of 597 Fg^{-1} compared to Z1-SC (412 Fg^{-1}) and Z2-SC (450 Fg^{-1}), since Z3-SC has both an EDLC as well as pseudocapacitive type behaviour, with broad Faradaic redox peaks. The mixed rectangular and pseudocapacitive formation of the Z3-SC is accounted for by the microporous architecture (1.18 cm^3 g^{-1}), faradaic interactions between lone electron pair of nitrogen functional groups with the cations in MESF, coordination of other oxygen functional species present on the biomass-derived electrode and biopolymer electrolyte surface (hydroxyl, carboxyl, and carbonyl) [17,43]. The higher C_{sp} of Z3-SC during lower potential sweep indicates the excellent charge propagation and dynamic property of with MESF. At a scan rate from 1 to 10 mV s^{-1}, Z3-SC (Fig. 10b) exhibits prominent box-type behaviour with pseudocapacitive redox peaks, inferring better electrochemical reversibility and redox activity between the electrode and electrolyte interface [10,13]. Further, it can be observed, even at a very high scan rate of 100 mV s^{-1} (Fig. S4), a good C_{sp} (208 F/g) is retained, compared to Z1-SC (84 F/g) and Z2-SC (100 F/g). The specific capacitance of Z-HPAC materials attained at various scan rate are shown in Fig. 10c. This high C_{sp} of Z3-SC can be ascribed the high electrochemically active surface area (ECSA), calculated (equation S6) from the electrochemical double-layer capacitance (C_{dl}), (Fig. S5). The calculated ECSA of Z3-SC is 3451.42 cm^2 at 0.5 V (Fig. 10b), reveals that the Z3 electrode is electrochemically active and has the potential to enhance the C_{sp} of the device. Also, the calculated (Eq. S7) interfacial capacitance (C_I) from C_{sp} and S_{BET} of Z3 is 0.323 F/cm^2 [60,61]. These excellent electrochemical performances are also due to the rapid ion transportation ability of MESF biopolymer electrolyte. The suppressed electrochemical performance of Z1 and Z2 biomass-derived electrodes with scan rate is attributed to the low surface area, inferior pore opening, porous blockage and low nitrogen content, which inhibits the ionic mobility during redox activity and hence, diminishes the specific capacitance [18].

Typical charge-discharge properties of the fabricated cells are studied at 1 mA current (Fig. 10d). Almost all the supercapacitors exhibited a quasi-isosceles triangle shape behaviour in the potential range of 0–0.8 V, a typical mixed performance of EDL and pseudocapacitive behaviour. The calculated C_{sp} (Eq. S2) is found to be much higher for Z3-SC (196 Fg^{-1}) compared to Z1-SC (105 Fg^{-1}) and Z2-SC (168 Fg^{-1}). The higher specific capacitance at lower current density is a reflection of the high surface area (1841 m^2 g^{-1}) and porous architecture (2.6 nm) of Z3 electrode. Besides, the wettability of MESF electrolyte tunes the oxygen-containing functional species to adsorb a number of ions and acts as a tunnel [22,23]. Thereby, the high nitrogen (2.1 at.wt%) content existing on the surface of Z3 biomass-derived electrode contributes more active sites for the ions traversed out of MESF, thus producing a higher capacitance at a lower current (0.5 mA). Interestingly, the obtained gravimetric specific capacitance (C_{sp}) is superior to the so far reported starch-based biopolymer electrolyte for all solid-state supercapacitors (Table 3). Mainly, on the basis of C_{sp}, the present work is found to be higher compared to all solid-state

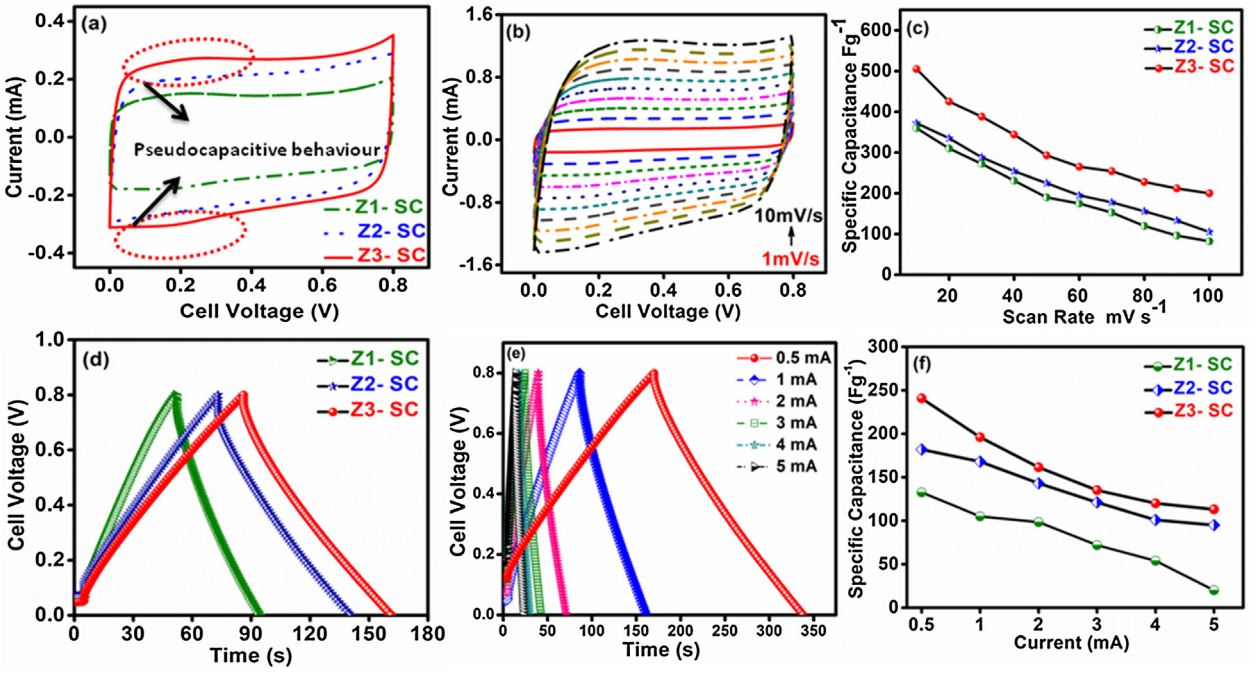

Fig. 10. a) Cyclic voltammogram of all fabricated cells at 2 mV s^{-1}, (b) CV of Z3-SC at 1 to 10 mV s^{-1}, (c) Scan rate vs. The specific capacitance of all the cells, (d) Charge-discharge curve of all the fabricated cells at 1 mA, (e) GCD curve of Z3-SC at different load current 0.5 to 5 mA, (f) Specific capacitance vs load current.

Table 3
Comparison of conductivity and specific capacitance of the present MESF biopolymer electrolyte with other reports using galvanostatic charge-discharge measurement.

Biopolymer Electrolytes	Conductivity	Specific Capacitance	Current	Reference
Corn starch/lithium acetate (LiAc)	$(1.04 \pm 0.10) \times 10^{-3}$ S cm^{-1}	33.00 F g^{-1}	0.1 mA cm^{-2}	[24]
Chitosan- Li+ /Ag^{+}	4.6 m S cm^{-1}	10 mF cm^{2}	1.8 mA cm^{-2}	[25]
Cellulose acetate/$LiClO_4$	4.9×10^{-3} S cm^{-1}	90 F g^{-1}	2 mA cm^{-2}	[27]
Starch-chitosan blend/NH_4Br	$(9.72 \pm 0.95) \times 10^{-5}$ S cm^{-1}	1172 mF g^{-1}	0.04 mA cm^{-2}	[29]
Corn Starch/$LiClO_4$/$BaTiO_3$	1.84×10^{-4} S cm^{-1}	16.22 F g^{-1}	4 mA cm^{-2}	[53]
Starch/Chitosan/NH_4Cl	$(5.11 \pm 1.60) \times 10^{-4}$ S cm^{-1}	3.4 4 F g^{-1}	0.063 mA	[62]
Corn starch/$BmImPF_6$/$LiPF_6$	$(1.47 \pm 0.02) \times 10^{-4}$ S cm^{-1}	37.07 F g^{-1}	0.5 Ag^{-1}	[63]
Potato starch (PS)/methyl cellulose(MC)/NH_4NO_3	$(1.26 \pm 0.1) \times 10^{-4}$ S cm^{-1}	31 F g^{-1}	0.2 mA cm^{-2}	[64]
Corn starch/$LiClO_4$	3.7×10^{-4} S cm^{-1}	127 F g^{-1}	2 mA cm^{-2}	[65]
KOH/Saturated mCel-membrane	0.325 S cm^{-1}	110 F g^{-1}	1 A g^{-1}	[66]
Hydroxyethyl cellulose/phosphoric acid (H_3PO_4)	4.1×10^{-3} S cm^{-1}	110 F g^{-1}	0.1 A g^{-1}	[67]
Methyl cellulose/NH_4NO_3/PEG	1.14×10^{-4} S cm^{-1}	38 F g^{-1}	1 mA	[68]
MESF	3.1×10^{-3} S cm^{-1}	240 F g^{-1}	0.5 mA	Present work

supercapacitors fabricated out of biopolymer electrolytes such as *Chitosan-Li^{+}/Ag^{+}* (10 mF cm^{2}), *Corn starch/$LiClO_4$/$BaTiO_3$* (16.22 F/g), *Corn starch/$BmImPF_6$/$LiPF_6$* (37.07 F/g), *Potato starch/methyl cellulose/NH_4NO_3* (31 F/g) and KOH/*mCelmembrane* (110 F/g) in recent.

The galvanostatic charge/discharge profile of Z3-SC at various current densities (0.5–5 mA) is also analysed (Fig. 10e), and the calculated C_{sp} values are given in Fig. 10f. The C_{sp} value of Z3-SC (113 Fg^{-1}) decreases with an increase in current (5 mA) due to limited diffusion mechanism occurring at the electrode/electrolyte interface. As bulk electrolytic ions would surround the concentration of the electrode/electrolyte interface, there would be insufficient time and space for the ions to move freely through. Also, the very small pores present a barrier and prevent the diffusion of ionic species, thus minimizing the energy storage capacity [26,68]. The decrease in C_{sp} with an increase in current suggests the rapid current-response ability and high charge-transfer stability of Z3-SC. Qualitatively, the obtained C_{sp} could be explained based on H^{+} ionic size and radii of hydrated cations with respect to the conductive electrolyte (H_2SO_4) present in the MESF. The following equations determine the area occupied by the hydration molecules (S_o) and the number of stacking layers (n_s) and the calculated [66] values are given in Table 4.

$$S_0 = \frac{C_s N \Delta V \sigma}{F} \tag{5}$$

$$n_s = \frac{S_o}{S_{BET}} \tag{6}$$

where N is Avogadro's number, σ is the cross-sectional area of the hydration molecule, and F is the Faraday constant. Table 4 infers that Z3-SC has higher S_0 (1 2 3) and n_s (0.06), thus providing higher surface accessibility for the solvated ions through MESF. As a result, high C_{sp} value is obtained even at the lower current.

Fig. 11a shows the Nyquist impedance plot of the symmetric cells, including Z1-SC, Z2-SC, and Z3-SC. The plot consists of a semi-circle in the high-frequency region, a Warburg line in the middle frequency region and a vertical spike in the low-frequency region. The semi-circle infers about the resistive nature, Warburg line represents the mixed behaviour of resistance as well as the capacitive nature of the supercapacitors [69–72]. While the vertical spike inclined at 90° infers the capacitive characteristic of the supercapacitor. The Nyquist plot for the supercapacitors is fitted with an equivalent electronic circuit through the following equation [73–76],

$$Z = R_s + \frac{1}{j_{wC_{dl}} + \frac{1}{R_{CT}+W_0}} - j\frac{1}{wC_F} \tag{7}$$

where R_s is the solution resistance, R_{ct} is the charge transfer resistance, C_{dl} is the double layer capacitance, and W_o is the finite-length Warburg diffusion element, which is expressed as, A/(j_ω) n, where A is the Warburg coefficient, ω is the angular frequency and n is an exponent, C_F is the Faradaic capacitance. The fitted values are given in Table 5. It is clear from the EIS spectra that the semicircle of Z3-SC has the smallest diameter due to the presence of functional groups, as explained in the XPS and FTIR spectra. Hence, Z3-SC experiences a low intrinsic resistance of 0.40 Ω compared Z1-SC (0.68 Ω) and Z2-SC (0.59 Ω) while traversing through the MESF electrolyte. Also, the charge transfer resistance (R_{ct}) of Z3-SC is found to be 8.8 Ω, inferring that the distance for ionic transportation in the Z3-SC is quite short and thus delivered a high C_{sp} of 228.8 Fg^{-1} (Eq. S8), which is in concordance with the C_{sp} (240 Fg^{-1}) obtained from GCD profile. Moreover, the W_o (15 Ω) suggests that the resistance for ionic diffusion from MESF at high frequency is low for Z3-SC. After 2000 charge/discharge cycles, the R_{ct} for Z3-SC is close to 11.9 Ω, which is due to the degradation of MESF biopolymer electrolyte film processes and the resistance offered onto Z-HPAC material (Fig. 11a (inset)).

Fig. 11b shows the Bode plot of Z3-SC representing the relation between frequency, phase angle and impedance. The phase angle of Z3-SC is found to be −74.81° higher than Z1-SC (−43.9°) and Z2-SC (−66.5°) shown in Fig. S6b, inferring the lowest intrinsic resistance of Z3-SC. Also, the impedance of Z3-SC is found to decrease with increasing frequency (Fig. 11b) in comparison with Z1-SC and Z2-SC (Fig. S6a), because of the low diffusion resistance of the MESF electrolyte. All solid-state Z3-SC device delivered a high real part impedance of 60 mF (Fig. 11c) compared to Z1-SC and Z2-SC of 26 mF and 42 mF, respectively (Fig. S6c), and exhibited a relaxation time of 5 s. (Fig. 11d), indicating its higher energy providing property compared to Z1-SC (12.5 *sec*) and Z2-SC (8 *sec*) shown in Fig. S6d. From the above impedance analysis, it is clear that Z3-SC has the potential as a supercapacitor.

Moreover, the Ragone plot (Fig. 12a), relates the specific energy (E) and the specific power (P) calculated using equation (S3 and S4), where, the specific energy is inversely proportional to specific power. The specific energy of Z3-SC at the specific power of 810 W kg^{-1} is 17 Wh kg^{-1}. Even at a high specific power of 3823 W kg^{-1}, the specific energy retains with 10 Wh kg^{-1}, compared to Z1-SC (1.2 Wh kg^{-1}) and Z2-SC (7.9 Wh kg^{-1}). The inset of Fig. 12a, reveals the practical applicability of the fabricated

Table 4
Faradaic capacitance due to each element presents in the sample according to XPS spectral analysis and BET analysis.

Sample Name	C_{sp} F g^{-1}	C_l F cm^{-2}	S_0	n_s
Z1-SC	105	0.25	53	0.03
Z2-SC	168	0.28	84	0.04
Z3-SC	196	0.32	123	0.06

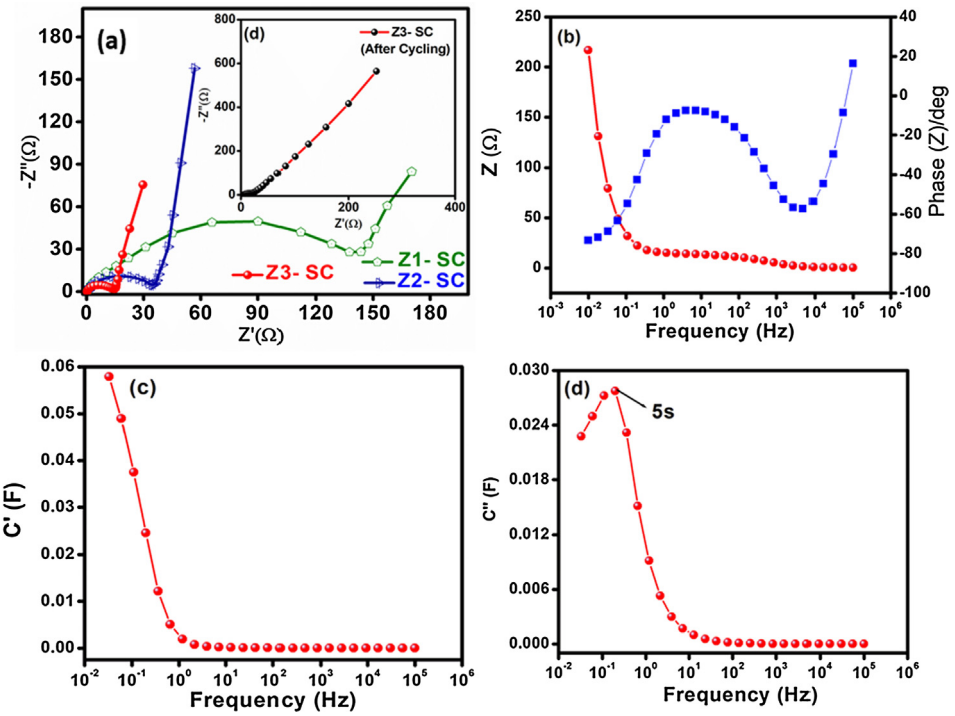

Fig. 11. (a) Nyquist Plot of Z1-SC, Z2-SC and Z3-SC, (b) Bode plot, (c) C′ vs frequency, and (d) C″ vs frequency of Z3-SC cell.

Table 5
Summarized equivalent circuit parameters from fitted Nyquist plot.

Supercapacitor	R_S (Ω)	R_{ct} (Ω)	C_{dl} (F g^{-1})	W_0 (Ω)	C_{sp} (F g^{-1})
Z1-SC	0.68	63	54.5×10^{-6}	52	149.12
Z2-SC	0.597	21	49.81×10^{-6}	18	146.62
Z3-SC	0.40	8.8	24.19×10^{-6}	15	228.81

device by a glowing red LED. The obtained specific energy of starch-based all-solid-state supercapacitor is comparatively higher than the biopolymer electrolyte in recent. Among wide search, all-solid-state supercapacitor using HPAC as electrodes, the KOH-saturated mCel-membrane as a polymer electrolyte exhibited maximum specific energy of 2.94 Wh kg^{-1} [66], Na-alginate hydrogel electrolyte attained specific energy of 8 Wh kg^{-1} [28].

Interestingly, Z3-SC demonstrated excellent cyclic stability (Fig. 12b) with a specific capacitance of 121 Fg^{-1} at 4 mA even after 2000, with a Columbic efficiency of 97% (equation S5). The 3% loss of efficiency is due to the constant exposure of the MESF at high cell voltages, which is a recoverable loss with minute optimization. With the above observation, it is noteworthy that Z3-SC possess a higher capacitive performance than the other two biomass-derived electrode materials. In order to identify the origin of better stability of the Z3-SC, the surface morphological features of the coated electrodes before and after cycling is studied. Fig. 13, shows the FE-SEM images of the coated Z3 electrode before (Fig. 13a) and after electrochemical stability (Fig. 13b). Interestingly, there is no significant morphological changes were observed on the FE-SEM images of the electrode even after 2000 cycles at a high discharge current of 4 mA. In the broader view, the surface of both the electrodes looks similar, that directly corroborates the stability of the electrode. Further, to identify the crystallinity of the Z3-SC electrode, the HRTEM and SAED analysis is performed after cycling, and the results are shown in Fig. 13(c and d). The observed well-defined lattice fringes with ring-shaped carbon layers from the HRTEM image infers that there is no structural defects occurred after cycling. Similarly, the measured d-spacing (0.35) corresponding to 002 planes is almost equal with the carbon measured before cycling. As well as the obtained SAED pattern (Fig. 13d) secured with a bright spot and broad ring, infers the unchanged amorphous nature of the carbon material even after stability, which is in concord with Fig. 7(d).

In detail, (i) the high surface area provides more space for the charge accumulation, (ii) the uniformly distributed micropores facilitates ease of ion migration, as well as the mesopores network shortens the diffusion path length of the ions, (iii) the high nitrogen and optimum oxygen species inherited on the carbon matrix enhances the hydrophilicity, wettability, and serve as an anchor to chemisorb ions to and fro from the MESF electrolyte. Subsequently, the increased conductivity and hydrophilicity of MESF helped the device with reduced solution resistance and acted as a good electrolytic reservoir and facilitated ionic movement at the electrode/electrolyte interface of the device. Therefore, the proper synchronization between Z3 material and MESF electrolyte as an all solid-state electric double layer capacitor delivered a superior specific capacity, energy density, power density and excellent cyclic stability. In conclusion, both the biomass-derived electrode and biopolymer electrolyte derived from starch delivered a maximum electrochemical performance with good energy and power densities. It is expected to deliver its maximum potential with minimum optimization effort to serve as a promising candidate in the electrochemical energy storage device.

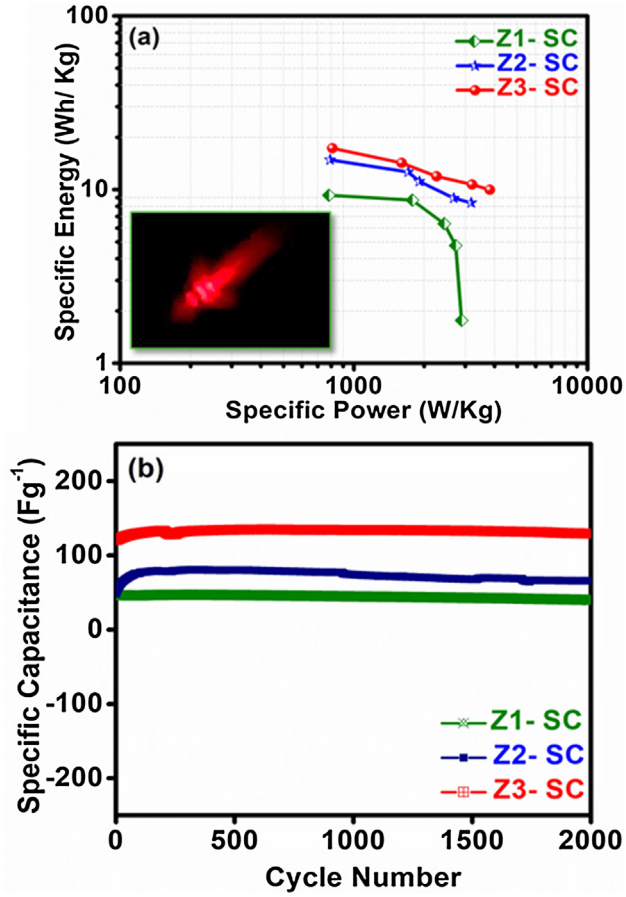

Fig. 12. (a) Ragone plot and (b) Cycling stability of all the cells.

4. Conclusions

This work focuses on improving the energy and power density of electric double layer capacitors (EDLC's) that demands the electrochemical energy storage community. Based on these criteria, to develop materials with low-cost, eco-friendlier yet highly efficient, biomass resources have opted. Successfully, a biomass-derived material out of AHS starch was produced via chemical activation with $ZnCl_2$, with different impregnation ratio. The optimized biomass-derived material is enriched with nitrogen species (2.1 at. wt.%), possessed a desirable high electrochemical surface area (1841 $m^2\ g^{-1}$) and porous architecture (1.18 $cm^3\ g^{-1}$). Especially, the *N*-functionalities organized on the activated carbon surface helped to improve the wettability of the electrode and hence yielded an excellent electrochemical performance. Besides, the fabricated flexible, transparent MESF electrolyte derived from *Manihot esculenta* starch, supported the mobility of ions during redox activity with its high conductivity (3.1×10^{-3} S cm^{-1}). MESF exposed to soil gradually degraded by the microorganisms was identified with the weight loss of 6% after 40 days under the soil. As a result, the fabricated green all-solid-state electric double layer capacitor showed a higher C_{sp} of 240 Fg^{-1} (0.5 mA), the specific energy of 17 Wh kg^{-1} and specific power of 3823 W kg^{-1}. Long cycling stability of 97% over 2000 cycles at 4 mA (130 Fg^{-1}) was obtained with the eco-friendlier device due to the hierarchical porosity. These parameters wholly address the superior electrochemical performance, sustainability, and stability of the fabricated EDLCs. Therefore, this biomass-derived electrode and biopolymer electrolyte materials developed from the starch base are found to be promising renewable candidates for supercapacitor based applications in future considering environmental concerns.

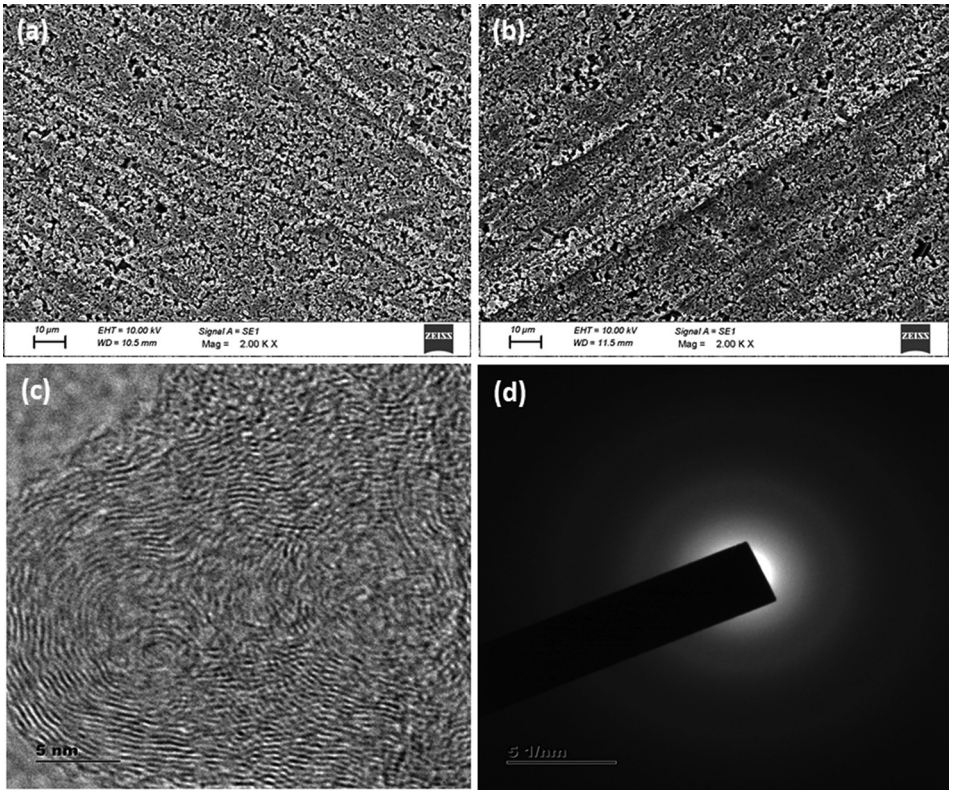

Fig. 13. FE-SEM image of Z3-SC electrodes (a) before and (b) after cycling stability test, (c) TEM and (d) HRTEM images (Inset: SAED pattern) of Z3-SC electrodes after stability.

Acknowledgements

Prof. Yun Sung Lee acknowledges the Ministry of Science, ICT and Future Planning of South Korea for providing a National Research Foundation of Korea (NRF) grant (No. 2019R1A4A2001527).

Appendix A. Supplementary material

Supplementary data to this article can be found online at https://doi.org/10.1016/j.jcis.2019.06.081.

References

[1] B.E. Conway, Electrochemical supercapacitors: scientific fundamentals and technological applications, Springer Sci. Buisness Media (2013) 1–698.
[2] Y. Gogotsi, R.M. Penner, Energy Storage in nanomaterials – capacitive, pseudocapacitive, or battery-like?, ACS Nano 12 (2018) 2081–2083
[3] P. Schlee, O. Hosseinaei, D. Baker, A. Landmér, P. Tomani, M.J. Mostazo-López, D. Cazorla-Amorós, S. Herou, M.-M. Titirici, From waste to wealth: from kraft lignin to free-standing supercapacitors, Carbon 145 (2019) 470–480.
[4] M. Sevilla, R. Mokaya, Energy storage applications of activated carbons: supercapacitors and hydrogen storage, Energy Environ. Sci. 7 (2014) 1250–1280.
[5] A.M. Zardkhoshoui, S.S.H. Davarani, Ultrahigh energy density supercapacitors based on facile synthesized Ni CoOH-rGO/NF hybrid electrodes, J. Alloys Comp. 769 (2018) 922–931.
[6] S. Cao, T. Qu, A. Zhang, Y. Zhao, A. Chen, N-doped hierarchical porous carbon with open-ended structure for high-performance supercapacitors, ChemElectroChem 6 (2019) 1696–1703.
[7] A.M. Zardkhoshoui, S.S.H. Davarani, Designing a flexible all-solid-state supercapacitor based on $CuGa_2O_4$ and FeP-rGO electrodes, J. Alloy. Compd. 773 (2019) 527–536.
[8] A.S. Yasin, M. Obaid, I.M. Mohamed, A. Yousef, N.A. Barakat, ZrO_2 nanofibers/activated carbon composite as a novel and effective electrode material for the enhancement of capacitive deionization performance, RSC Adv. 7 (2017) 4616–4626.
[9] J. Cao, C. Zhu, Y. Aoki, H. Habazaki, Starch-derived hierarchical porous carbon with controlled porosity for high-performance supercapacitors, ACS Sustain. Chem. Eng. 6 (2018) 7292–7303.
[10] X. Zhao, H. Zhou, V.S. Sikarwar, M. Zhao, A.-H.A. Park, P.S. Fennell, L. Shen, L.-S. Fan, Biomass-based chemical looping technologies: the good, the bad and the future, Energy Environ. Sci. 10 (2017) 1885–1910.
[11] D.I. Abouelamaiem, G. He, I. Parkin, T.P. Neville, A.B. Jorge, S. Ji, R. Wang, M.-M. Titirici, P.R. Shearing, D.J.L. Brett, Synergistic relationship between the three-dimensional nanostructure and electrochemical performance in biocarbon supercapacitor electrode materials, Sustain. Energy Fuels 2 (2018) 772–785.
[12] Q. Chen, J. Sun, Z. Wang, Z. Zhao, Y. Zhang, Y. Liu, L. Hou, C. Yuan, Sustainable rose multiflora derived nitrogen/oxygen-enriched micro-/mesoporous carbon as a low-cost competitive electrode towards high-performance electrochemical supercapacitors, RSC Adv. 8 (2018) 9181–9191.
[13] Q. Zhang, K. Han, S. Li, M. Li, J. Li, K. Ren, Synthesis of garlic skin-derived 3D hierarchical porous carbon for high-performance supercapacitors, Nanoscale 10 (2018) 2427–2437.
[14] W. Hong, L. Wang, K. Liu, X. Han, Y. Zhou, P. Gao, R. Ding, E. Liu, Asymmetric supercapacitor constructed by self-assembled camellia-like BiOCl and activated carbon microspheres derived from sweet potato starch, J. Alloy. Compd. 746 (2018) 292–300.
[15] D. Guo, R. Xin, Y. Wang, W. Jiang, Q. Gao, G. Hu, M. Fan, N-doped carbons with hierarchically micro- and mesoporous structure derived from sawdust for high-performance supercapacitors, Micropor. Mesopor. Mater. 279 (2019) 323–333.
[16] X. Tian, S. Zhu, J. Peng, Y. Zuo, G. Wang, X. Guo, N. Zhao, Y. Ma, L. Ma, Synthesis of micro- and mesoporous carbon derived from cellulose as an electrode material for supercapacitors, Electrochim. Acta 241 (2017) 170–178.
[17] K. Sun, S. Yu, Z. Hu, Z. Li, G. Lei, Q. Xiao, Y. Ding, Oxygen-containing hierarchically porous carbon materials derived from wild jujube pit for high-performance supercapacitor, Electrochim. Acta 231 (2017) 417–428.
[18] V. Khairnar, S. Jaybhaye, C.-C. Hu, R. Afre, T. Soga, M. Sharon, M. Sharon, Development of supercapacitors using porous carbon materials synthesized from plant-derived precursors, Carbon Lett. 9 (2008) 188–194.
[19] P. Rupa Kasturi, R. Kalai Selvan, Y.S. Lee, Pt-decorated Artocarpus heterophyllus seed derived carbon as an anode catalyst for DMFC application, RSC Adv. 6 (2016) 62680–62694.
[20] P. Kalyani, A. Anitha, On the (pseudo) capacitive performance of jackfruit seed carbon, Int. J. Res. Eng. Technol. 3 (2014) 225–238.
[21] C. Zhong, Y. Deng, W. Hu, J. Qiao, L. Zhang, J. Zhang, A review of electrolyte materials and compositions for electrochemical supercapacitors, Chem. Soc. Rev. 44 (2015) 7484–7539.
[22] V. Selvanathan, A.D. Azzahari, A.A. Abd Halim, R. Yahya, Ternary natural deep eutectic solvent (NADES) infused phthaloyl starch as cost efficient quasi-solid gel polymer electrolyte, Carbohydr. Polym. 167 (2017) 210–218.
[23] C. Saldías, D.D. Díaz, S. Bonardd, C. Soto-Marfull, A. Cordoba, S. Saldías, C. Quezada, D. Radic, Á. Leiva, In situ preparation of film and hydrogel bio-nanocomposites of chitosan/fluorescein-copper with catalytic activity, Carbohydr. Polym. 180 (2018) 200–208.
[24] M.F. Shukur, R. Ithnin, M.F.Z. Kadir, Electrical characterization of corn starch-LiOAc electrolytes and application in electrochemical double layer capacitor, Electrochim. Acta 136 (2014) 204–216.
[25] L. Cao, M. Yang, D. Wu, F. Lyu, Z. Sun, X. Zhong, H. Pan, H. Liu, Z. Lu, Biopolymer-chitosan based supramolecular hydrogels as solid-state electrolytes for electrochemical energy storage, Chem. Commun. 53 (2017) 1615–1618.
[26] X. Du, Z. Zhang, W. Liu, Y. Deng, Nanocellulose-based conductive materials and their emerging applications in energy devices - a review, Nano Energy 35 (2017) 299–320.
[27] M. Selvakumar, D.K. Bhat, $LiClO_4$ doped cellulose acetate as biodegradable polymer electrolyte for supercapacitors, J. Appl. Polym. Sci. 110 (2008) 594–602.
[28] J. Zeng, L. Wei, X. Guo, Bio-inspired high-performance solid-state supercapacitors with the electrolyte, separator, binder and electrodes entirely from kelp, J. Mater. Chem. A 5 (2017) 25282–25292.
[29] M.F. Shukur, R. Ithnin, M.F.Z. Kadir, Protonic transport analysis of starch-chitosan blend based electrolytes and application in electrochemical device, Mol. Cryst. Liq. Cryst. 603 (2014) 52–65.
[30] C. Wang, D. Wu, H. Wang, Z. Gao, F. Xu, K. Jiang, A green and scalable route to yield porous carbon sheets from biomass for supercapacitors with high capacity, J. Mater. Chem. A 6 (2018) 1244–1254.
[31] A.J. Gross, M. Holzinger, S. Cosnier, Buckypaper bioelectrodes: emerging materials for implantable and wearable biofuel cells, Energy Environ. Sci. 11 (2018) 1670–1687.
[32] P. Zhang, X. Song, C. Yu, J. Gui, J. Qiu, Biomass-derived carbon nanospheres with turbostratic structure as metal-free catalysts for selective hydrogenation of o-chloronitrobenzene, ACS Sustain. Chem. Eng. 5 (2017) 7481–7485.
[33] Z. Liu, Y. Huang, G. Zhao, Preparation and characterization of activated carbon fibers from liquefied wood by $ZnCl_2$ activation, BioResources 11 (2016) 3178–3190.
[34] S. Yan, J. Lin, P. Liu, Z. Zhao, J. Lian, W. Chang, L. Yao, Y. Liu, H. Lin, S. Han, Preparation of nitrogen-doped porous carbons for high-performance supercapacitor using biomass of waste lotus stems, RSC Adv. 8 (2018) 6806–6813.
[35] H. Okuda, R.J. Young, D. Wolverson, F. Tanaka, G. Yamamoto, T. Okabe, Investigating nanostructures in carbon fibres using Raman spectroscopy, Carbon 130 (2018) 178–184.
[36] S.K. Theydan, Effect of process variables, adsorption kinetics and equilibrium studies of hexavalent chromium removal from aqueous solution by date seeds and its activated carbon by $ZnCl_2$, Iraqi J. Chem. Petrol. Eng. 19 (2018) 1–12.
[37] Y.N. Sun, Z.Y. Sui, X. Li, P.W. Xiao, Z.X. Wei, B.H. Han, Nitrogen-doped porous carbons derived from polypyrrole-based aerogels for gas uptake and supercapacitors, ACS Appl. Nano Mater. 1 (2018) 609–616.
[38] L. Yan, J. Yu, J. Houston, N. Flores, H. Luo, Biomass-derived porous nitrogen-doped carbon for electrochemical devices, Green Energy Environ. 2 (2017) 84–99.
[39] L. Li, F. Sun, J. Gao, L. Wang, X. Pi, G. Zhao, Broadening the pore size of coal-based activated carbon via a washing-free chem-physical activation method for high-capacity dye adsorption, RSC Adv. 8 (2018) 14488–14499.
[40] N. Mohammed, N. Grishkewich, K.C. Tam, Cellulose nanomaterials: promising sustainable nanomaterials for application in water/wastewater treatment processes, Environ. Sci. Nano 5 (2018) 623–658.
[41] L.C. Giovana, L.F.C. Maria, A.V. Germán, D.A.S.P. José, F.M.I. Cristina, Evaluation of extraction method on the structure and physicochemical properties of starch from seeds of two jackfruit varieties, Starch - Stärke 69 (2017) 1700078.
[42] B. Ashourirad, M. Demir, R.A. Smith, R.B. Gupta, H.M. El-Kaderi, Rapid transformation of heterocyclic building blocks into nanoporous carbons for high-performance supercapacitors, RSC Adv. 8 (2018) 12300–12309.
[43] Z. Sun, J. Liao, B. Sun, M. He, X. Pan, J. Zhu, C. Shi, Y. Jiang, Nitrogen self-doped porous carbon materials derived from a new biomass source for highly stable supercapacitors, Int. J. Electrochem. Sci. 12 (2017) 12084–12097.
[44] Z. Xiao, W. Chen, K. Liu, P. Cui, D. Zhan, Porous biomass carbon derived from peanut shells as electrode materials with enhanced electrochemical performance for supercapacitors, Int. J. Electrochem. Sci. 13 (2018) 5370–5381.
[45] K.O. Köse, B. Pişkin, M.K. Aydınol, Chemical and structural optimization of $ZnCl_2$ activated carbons via high temperature CO_2 treatment for EDLC applications, Int. J. Hydrogen Energy 43 (2018) 18607–18616.
[46] Q. Yao, H. Wang, C. Wang, C. Jin, Q. Sun, One step construction of Nitrogen-carbon derived from bradyrhizobium japonicum for supercapacitor applications with a soybean leaf as a separator, ACS Sustain. Chem. Eng. 6 (2018) 4695–4704.
[47] J.R. García, U. Sedran, M.A.A. Zaini, Z.A. Zakaria, Preparation, characterization, and dye removal study of activated carbon prepared from palm kernel shell, Environ. Sci. Pollut. Res. 25 (2018) 5076–5085.
[48] D. Xu, B. Wang, Q. Wang, S. Gu, W. Li, J. Jin, C. Chen, Z. Wen, High-strength internal cross-linking bacterial cellulose-network-based gel polymer

electrolyte for dendrite-suppressing and high-rate lithium batteries, ACS Appl. Mater. Interf. 10 (2018) 17809–17819.
[49] Y.M. Yusof, M.F.Z. Kadir, Electrochemical characterizations and the effect of glycerol in biopolymer electrolytes based on methylcellulose-potato starch blend, Mol. Cryst. Liq. Cryst. 627 (2016) 220–233.
[50] H. Ji, X. Song, Z. Shi, C. Tang, L. Xiong, W. Zhao, C. Zhao, Reinforced-concrete structured hydrogel microspheres with ultrahigh mechanical strength, restricted water uptake, and superior adsorption capacity, ACS Sustain. Chem. Eng. 6 (2018) 5950–5958.
[51] X. Tang, Y.H. Lui, A.R. Merhi, B. Chen, S. Ding, B. Zhang, S. Hu, Redox-active hydrogel polymer electrolytes with different ph values for enhancing the energy density of the hybrid solid-state supercapacitor, ACS Appl. Mater. Interf. 9 (2017) 44429–44440.
[52] D.R. Lu, C.M. Xiao, S.J. Xu, Starch-based completely biodegradable polymer materials, eXPRESS Polym. Lett. 3 (2009) 366–375.
[53] K.H. Teoh, C.S. Lim, C.W. Liew, S. Ramesh, Preparation and performance analysis of barium titanate incorporated in corn starch-based polymer electrolytes for electric double layer capacitor application, J. Appl. Polym. Sci. 133 (2016). 43275 (1–8).
[54] M.H. Khanmirzaei, S. Ramesh, K. Ramesh, Polymer electrolyte based dye-sensitized solar cell with rice starch and 1-methyl-3-propylimidazolium iodide ionic liquid, Mater. Des. 85 (2015) 833–837.
[55] M.F. Shukur, R. Ithnin, M.F.Z. Kadir, Electrical properties of proton conducting solid biopolymer electrolytes based on starch–chitosan blend, Ionics 20 (2014) 977–999.
[56] M.F. Shukur, F. Sonsudin, R. Yahya, Z. Ahmad, R. Ithnin, M.F.Z. Kadir, Electrical properties of starch based silver ion conducting solid biopolymer electrolyte, Adv. Mater. Res. 701 (2013) 120–124.
[57] S.C. Pang, C.L. Tay, S.F. Chin, Starch-based gel electrolyte thin films derived from native sago (Metroxylon sagu) starch, Ionics 20 (2014) 1455–1462.
[58] R. Singh, P.K. Singh, S.K. Tomar, B. Bhattacharya, Synthesis, characterization, and dye-sensitized solar cell fabrication using solid biopolymer electrolyte membranes, High Perform. Polym. 28 (2016) 47–54.
[59] N. Hataf, P. Ghadir, N. Ranjbar, Investigation of soil stabilization using chitosan biopolymer, J. Cleaner Prod. 170 (2018) 1493–1500.
[60] A.M. Zardkhoshoui, S.S.H. Davarani, Synthesis of $NiGa_2S_4$-rGO on nickel foam as advanced electrode for flexible solid-state supercapacitor with superior energy density, J. Coll. Interf. Sci. 535 (2019) 195–204.
[61] L. Zhang, L. Xu, Y. Zhang, X. Zhou, L. Zhang, A. Yasin, L. Wang, K. Zhi, Facile synthesis of bio-based nitrogen- and oxygen-doped porous carbon derived from cotton for supercapacitors, RSC Adv. 8 (2018) 3869–3877.
[62] M.F. Shukur, M.F.Z. Kadir, Hydrogen ion conducting starch-chitosan blend based electrolyte for application in electrochemical devices, Electrochim. Acta 158 (2015) 152–165.
[63] C.W. Liew, S. Ramesh, Electrical, structural, thermal and electrochemical properties of corn starch-based biopolymer electrolytes, Carbohydr. Polym. 124 (2015) 222–228.
[64] M.H. Hamsan, M.F. Shukur, M.F.Z. Kadir, NH_4NO_3 as charge carrier contributor in glycerolized potato starch-methyl cellulose blend-based polymer electrolyte and the application in electrochemical double-layer capacitor, Ionics 23 (2017) 3429–3453.
[65] Y.N. Sudhakar, M. Selvakumar, Lithium perchlorate doped plasticized chitosan and starch blend as biodegradable polymer electrolyte for supercapacitors, Electrochim. Acta 78 (2012) 398–405.
[66] D. Zhao, C. Chen, Q. Zhang, W. Chen, S. Liu, Q. Wang, Y. Liu, J. Li, H. Yu, High performance flexible, solid-state supercapacitors based on a renewable and biodegradable mesoporous cellulose membrane, Adv. Energy Mater. 7 (2017) 1700739.
[67] Y.N. Sudhakar, M. Selvakumar, D. Krishna Bhat, Preparation and characterization of phosphoric acid-doped hydroxyethyl cellulose electrolyte for use in supercapacitor, Mater. Renew. Sustain. Energy 4 (2015) 2–9.
[68] N.E.A. Shuhaimi, L.P. Teo, H.J. Woo, S.R. Majid, A.K. Arof, Electrical double-layer capacitors with plasticized polymer electrolyte based on methyl cellulose, Polym. Bull. 7 (2012) 807–826.
[69] A.M. Zardkhoshoui, S.S.H. Davarani, Flexible asymmetric supercapacitors based on CuO@MnO_2-rGO and MoS_2-rGO with ultrahigh energy density, J. Electroanal. Chem. 827 (2018) 221–229.
[70] H.-B. Huang, Y. Wang, W.-B. Jiao, F.-Y. Cai, M. Shen, S.-G. Zhou, H.-L. Cao, J. Lü, R. Cao, Lotus-leaf-derived activated-carbon-supported nano-CdS as energy-efficient photocatalysts under visible irradiation, ACS Sustain. Chem. Eng. 6 (2018) 7871–7879.
[71] A. Shah, A. Zahid, H. Subhan, A. Munir, F.J. Iftikhar, M. Akbar, Heteroatom-doped carbonaceous electrode materials for high performance energy storage devices, Sustain. Energy Fuels 2 (2018) 1398–1429.
[72] A.M. Zardkhoshoui, S.S.H. Davarani, All-solid-state, flexible, ultrahigh performance supercapacitors based on the Ni-Al LDH-rGO electrodes, J. Alloy. Compd. 750 (2018) 515–522.
[73] A.M. Zardkhoshoui, S.S.H. Davarani, M. Hashemi, Fabrication of cobalt gallium oxide with zinc iron oxide on nickel foam for a high-performance asymmetric supercapacitor, New J. Chem. 43 (2019) 4590–4598.
[74] A.M. Zardkhoshoui, S.S.H. Davarani, A.A. Asgharinezhad, Designing graphene-wrapped $NiCo_2Se_4$ microspheres with petal-like FeS_2 toward flexible asymmetric all-solid-state supercapacitors, Dalton Trans. 48 (2019) 4274–4282.
[75] A.M. Zardkhoshoui, S.S.H. Davarani, M.M. Ashtiani, M. Sarparast, Designing an asymmetric device based on graphene wrapped yolk–double shell $NiGa_2S_4$ hollow microspheres and graphene wrapped FeS_2–$FeSe_2$ core–shell cratered spheres with outstanding energy density, J. Mater. Chem. A 7 (2019) 10282–10292.
[76] A.M. Zardkhoshoui, S.S.H. Davarani, M.M. Ashtiani, M. Sarparast, High-Performance Energy Storage Device Based on Triple-Shelled Cobalt Gallium Oxide Hollow Spheres and Graphene Wrapped Copper Iron Disulfide Porous Spheres, ACS Sustain. Chem. Eng. 7 (2019) 7908–7917.